


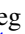




# Andromeda's Parachute: A Bright Quadruply Lensed Quasar at $z = 2.377$

Kate H. R. Rubin<sup>1</sup> , John M. O'Meara<sup>2</sup> , Kathy L. Cooksey<sup>3</sup>, Mateusz Matuszewski<sup>4</sup>, Luca Rizzi<sup>5</sup> , Greg Doppmann<sup>5</sup>, Shui Kwok<sup>5</sup>, D. Christopher Martin<sup>4</sup>, Anna M. Moore<sup>6</sup>, Patrick Morrissey<sup>4</sup>, and James D. Neill<sup>4</sup> 

<sup>1</sup> Department of Astronomy, San Diego State University, San Diego, CA 92182, USA; [krubin@sdsu.edu](mailto:krubin@sdsu.edu)

<sup>2</sup> Department of Chemistry and Physics, Saint Michael's College, One Winooski Park, Colchester, VT 05439, USA

<sup>3</sup> Department of Physics & Astronomy, University of Hawai'i at Hilo, 200 West Kāwili Street, Hilo, HI 96720, USA

<sup>4</sup> Cahill Center for Astrophysics, California Institute of Technology, 1216 East California Boulevard, Mail Code 278-17, Pasadena, California 91125, USA

<sup>5</sup> W.M. Keck Observatory, 65-1120 Mamalahoa Highway, Kamuela, HI 96743, USA

<sup>6</sup> Research School of Astronomy and Astrophysics, The Australian National University, Canberra, ACT 2611, Australia

Received 2017 July 17; revised 2018 February 5; accepted 2018 February 9; published 2018 June 1

## Abstract

We present Keck Cosmic Web Imager spectroscopy of the four putative images of the lensed quasar candidate J014710+463040 recently discovered by Berghea et al. The data verify the source as a quadruply lensed, broad absorption-line quasar having  $z_S = 2.377 \pm 0.007$ . We detect intervening absorption in the Fe II  $\lambda\lambda 2586, 2600$ , Mg II  $\lambda\lambda 2796, 2803$ , and/or C IV  $\lambda\lambda 1548, 1550$  transitions in eight foreground systems, three of which have redshifts consistent with the photometric-redshift estimate reported for the lensing galaxy ( $z_L \approx 0.57$ ). The source images probe these absorbers over transverse physical scales of  $\approx 0.3$ –22 kpc, permitting assessment of the variation in metal-line equivalent width  $W_r$  as a function of sight-line separation. We measure differences in  $W_{r,2796}$  of  $<40\%$  across most of the sight-line pairs subtending 8–22 kpc, suggestive of a high degree of spatial coherence for the Mg II-absorbing material.  $W_{r,2600}$  varies by  $>50\%$  over the same scales across the majority of sight-line pairs, while C IV absorption exhibits a wide range in  $W_{r,1548}$  differences of  $\approx 5\%$ –80% within transverse distances of  $\lesssim 3$  kpc. These spatial variations are consistent with those measured in intervening absorbers detected toward lensed quasars drawn from the literature, in which  $W_{r,2796}$  and  $W_{r,1548}$  vary by  $\leq 20\%$  in  $35 \pm 7\%$  and  $47 \pm 6\%$  of sight lines separated by  $< 10$  kpc, respectively. J014710+463040 is one of only a handful of  $z > 2$  quadruply lensed systems for which all four source images are very bright ( $r = 15.4$ –17.7 mag) and are easily separated in ground-based seeing conditions. As such, it is an ideal candidate for higher-resolution spectroscopy probing the spatial variation in the kinematic structure and physical state of intervening absorbers.

**Key words:** gravitational lensing; strong – intergalactic medium – quasars: absorption lines – techniques: imaging spectroscopy

## 1. Introduction

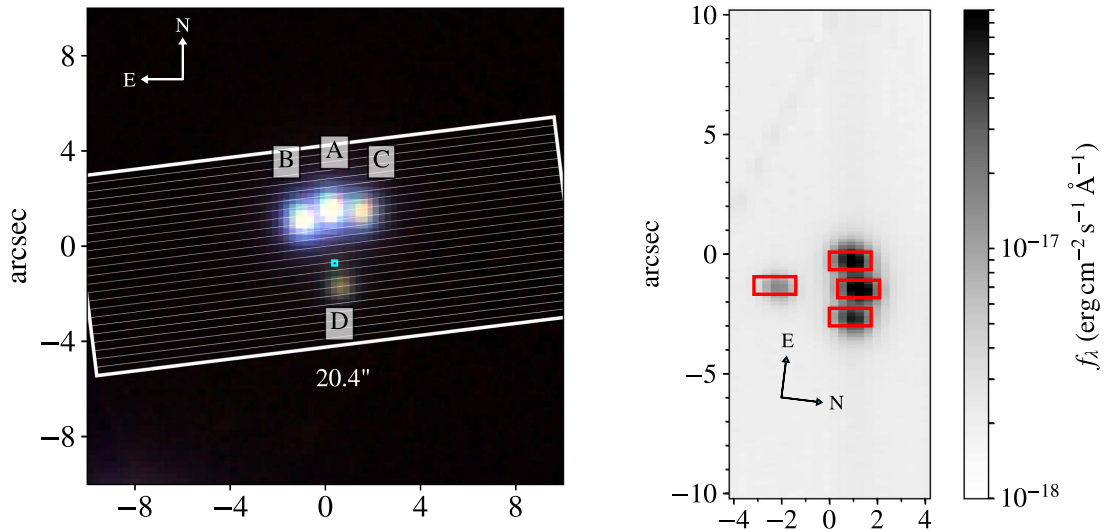
Strong gravitational lensing of high-redshift quasars has proven to be a powerful astrophysical and cosmological tool for a myriad of applications. Experiments range from high-fidelity spectroscopy probing the structure of the broad-line region surrounding the host active galactic nuclei (e.g., Nemiroff 1988; Sluse et al. 2012) to time domain observations constraining cosmological parameters (e.g., Bonvin et al. 2017). However, the brightest and most valuable of these sources are rare. Candidate lensed quasars may now be efficiently identified via color and morphological selection techniques (e.g., Schechter et al. 2017) or using variability criteria (e.g., Kochanek et al. 2006) in wide-field optical and near-infrared imaging surveys (e.g., Inada et al. 2012; Diehl et al. 2014; Shanks et al. 2015). Follow-up spectroscopy is then always required to confirm the nature of the system.

Recently, Berghea et al. (2017) identified a quadruply lensed quasar candidate in imaging obtained by the Panoramic Survey Telescope and Rapid Response System (hereafter PS1; Chambers et al. 2016). Astrometry of the components implies distances between source images of  $\approx 1''3$ – $3''4$ . They reported satisfactory spectral energy distribution (SED) fits to the source photometry for quasar templates at both  $z_S = 0.820^{+0.018}_{-0.014}$  and  $z_S \approx 2.6$ . Additionally, they found that SED modeling of the photometry of the prospective lens galaxy yields a best-fit redshift of  $z_L = 0.57^{+0.20}_{-0.13}$ .

In principle, images of a source QSO at  $z_S \approx 2.6$  lensed by a foreground system at  $z_L = 0.57$  and separated by  $1''3$ – $3''4$  probe physical scales of  $\approx 0.5$ –25 kpc at  $z \approx 0.5$ –2. Such a configuration is highly valuable for the study of the transverse small-scale coherence of circumgalactic medium (CGM) absorption. The brightness of this particular candidate ( $r = 15.4$ –17.7 mag) and relatively large separation of the source images enable high-signal-to-noise (S/N) spectroscopy with maximum efficiency.

In this paper, we present spectroscopy from the recently commissioned Keck Cosmic Web Imager (KCWI; P. Morrissey et al. 2018, in preparation) confirming that this system (J014710+463040) is a quadruply lensed quasar at  $z_S = 2.377$ . We then analyze intervening metal-line absorption systems detected along these sight lines in conjunction with additional systems collected from the literature for constraints on their spatial coherence. Given the source image configuration and its location on the sky, we refer to this object as Andromeda's Parachute.<sup>7</sup> We adopt the WMAP5 cosmology ( $H_0 = 70.2 \text{ km s}^{-1} \text{ Mpc}^{-1}$ ,  $\Omega_M = 0.277$ , and  $\Omega_\Lambda = 0.723$ ; Komatsu et al. 2009) throughout this work unless otherwise specified.

<sup>7</sup> The NASA Apollo and Orion command modules and SpaceX Dragon capsule (source image D) made ocean landings with the aid of a parachute system (A–C).



**Figure 1.** Left: PS1 *giy* color image (Chambers et al. 2016) of the lensed quasar system. Each source image is labeled A–D (brightest to faintest) as in Bergeha et al. (2017). The small cyan square shows the approximate location of the lensing galaxy. The thin white lines show the width of each  $0''.35$  image slicer within the KCWI footprint. Right: KCWI image of the target obtained from one 600 s exposure. The grayscale shows the flux density averaged over the wavelength range  $4200 \text{ \AA} < \lambda_{\text{obs}} < 4300 \text{ \AA}$  in each spaxel of the rectified datacube. The red boxes indicate the placement and size of the apertures used to generate the 1D spectra shown in Figure 2.

## 2. Observations

We observed J014710+463040 with KCWI on the night of 2017 June 21 UT. The instrument was configured with the small image slicer and BL grating, providing a spatial sampling of  $0''.35 \text{ pix}^{-1}$  and a spectral resolution of  $\mathcal{R} \approx 5000$ . The field-of-view of KCWI in this configuration is  $8''.4 \times 20''.4$ , permitting simultaneous spectroscopy of all four source images in a single pointing (e.g., Wisotzki et al. 2003). PS1 imaging of the target<sup>8</sup> and the placement of the KCWI footprint are shown in Figure 1 (left panel). The image slices were oriented at a position angle of  $97^\circ.1$ . We obtained two exposures of 600 s each while the target was at airmass  $\approx 1.5$ – $1.6$ .

The data were reduced using the publicly available `kderp` package.<sup>9</sup> We used in-house software to rectify the curved object traces along the cube resulting from differential atmospheric dispersion. The final rectified KCWI image, averaged over the wavelength range  $4200 \text{ \AA} < \lambda_{\text{obs}} < 4300 \text{ \AA}$ , is shown in the right-hand panel of Figure 1.

To extract 1D spectra from this rectified cube, we performed a simple sum of the flux over the spatial dimensions in  $5 \times 5$  pixel sub-cubes centered on each source image (see red apertures in Figure 1, right panel). A sky spectrum was extracted in the same manner from an off-source region of the datacube and was subtracted from each of the on-source spectra. We then co-added the 1D spectra extracted from the two 600 s exposures for each source image. These co-added 1D spectra are shown in Figure 2, and have median S/N per pixel measured redward of the quasar  $\text{Ly}\alpha$  emission line of  $\sim 180$ ,  $\sim 160$ ,  $\sim 130$ , and  $\sim 45$  in images A, B, C, and D, respectively.

<sup>8</sup> We note a small offset of approximately  $0''.18$  W and  $0''.22$  N between the *Gaia* position listed for component D in Bergeha et al. (2017) and the centroid of this source image in the PS1 imaging. We have adjusted the location of the symbol marking the lensing galaxy in Figure 1 accordingly.

<sup>9</sup> See <https://github.com/kcwidev/kderp>.

## 3. Spectroscopic Analysis

Figure 2 makes evident that each source image originates from the same high-redshift quasar. The complex absorption features blanketing the quasar’s broad  $\text{Ly}\alpha$ ,  $\text{Si IV}$ , and  $\text{C IV}$  emission lines (at  $\lambda_{\text{obs}} \sim 4100 \text{ \AA}$ ,  $4700 \text{ \AA}$ , and  $5150 \text{ \AA}$ ) indicate that it belongs to the broad absorption-line (BAL) quasar subclass (Weymann et al. 1991).

### 3.1. Redshift of J014710+463040

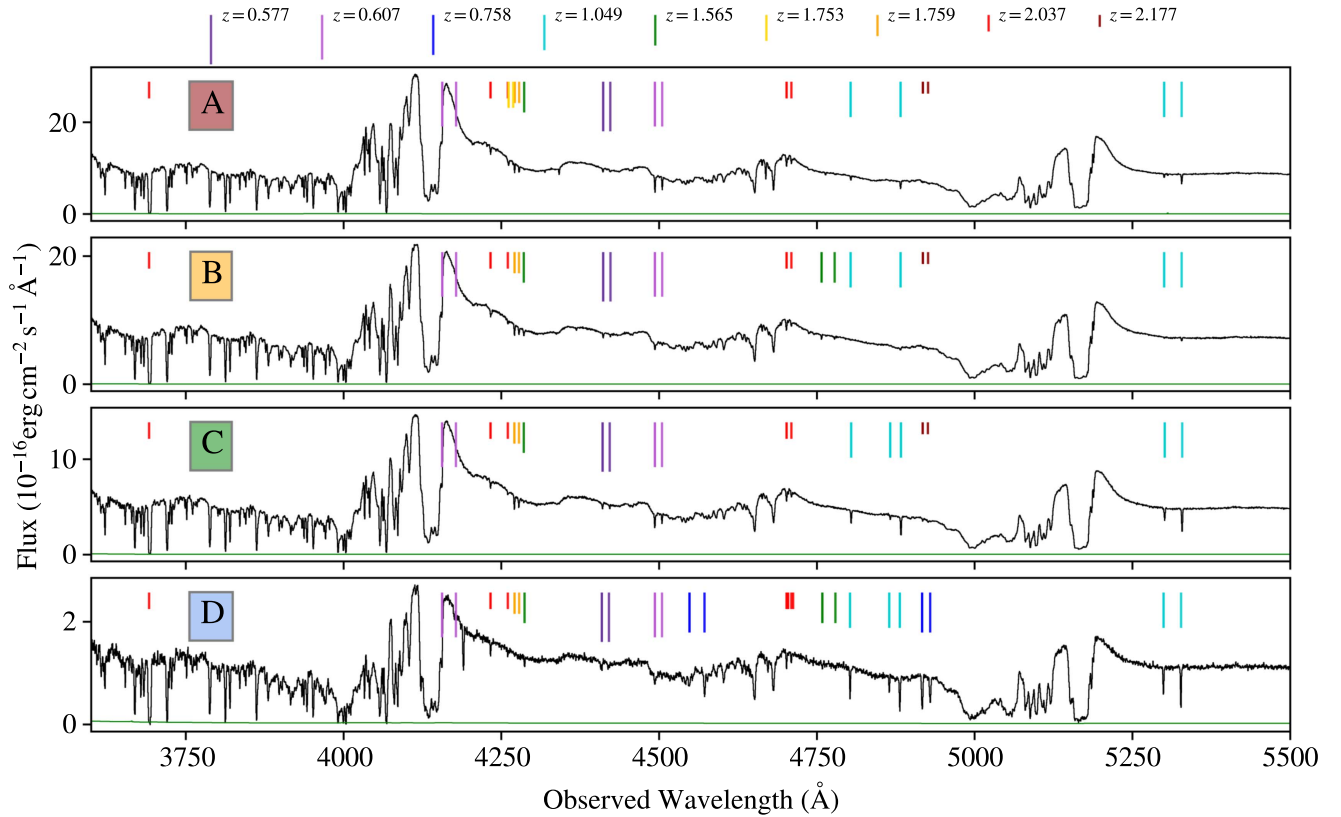
To measure the quasar redshift, we cross-correlate the quasar template used in Hewett & Wild (2010) with each of the four spectra shown in Figure 2. Given the BAL nature of J014710+463040, we exclude the template blueward of restframe  $\lambda = 1250 \text{ \AA}$  (i.e., the  $\text{Ly}\alpha$  and  $\text{N V}$  QSO emission lines). We fit a Gaussian to the peak of the cross-correlation, adopting the best-fit Gaussian centroid as the redshift for each source image. We adopt the mean and sample standard deviation of the four measurements as the source redshift  $z_s = 2.377 \pm 0.007$ . Observations at longer wavelengths are needed to constrain the redshift to higher precision.

### 3.2. Intervening Absorption

We visually inspected each spectrum to identify foreground metal-line absorption, focusing in particular on the identification of  $\text{C IV } \lambda\lambda 1548, 1550$ ,  $\text{Al II } \lambda 1670$ ,  $\text{Al III } \lambda\lambda 1854, 1862$ ,  $\text{Mg II } \lambda\lambda 2796, 2803$ , and  $\text{Fe II } \lambda\lambda 2586, 2600$  transitions known to arise in collisionally ionized or photoionized diffuse media at temperatures of  $\sim 10^{4-5} \text{ K}$  (Bergeron & Stasińska 1986). We used the Python package `linetools`<sup>10</sup> to interactively fit a spline function to the continuum of each quasar image and produce continuum-normalized spectra. We then used the interactive `IGMGuesses` GUI available with the `pyigm` Python package<sup>11</sup> to select velocity ranges for each absorber and fit

<sup>10</sup> <http://linetools.readthedocs.io/en/latest/index.html>

<sup>11</sup> <http://pyigm.readthedocs.io/en/latest/index.html>



**Figure 2.** Extracted 1D spectra of the four images indicated in Figure 1 demonstrating that the source is a lensed BAL quasar at  $z_S = 2.377$ . Intrinsic absorption features extend up to  $\approx 10,000$  km  $s^{-1}$  blueward of each emission line (e.g., C IV at  $\lambda_{\text{obs}} \approx 5200 \text{ \AA}$ ). Intervening metal-line absorption systems are indicated with vertical colored marks, and are in most cases detected along all four sight lines.

Voigt profiles to determine the wavelength centroid ( $z_{\text{abs}}$ ). We measured the rest equivalent width ( $W_r$ ) of each line using a boxcar sum of the flux decrement over the selected velocity range.

We summarize these systems in Table 1 and indicate them with vertical lines in Figure 2. Table 1 also indicates transitions affected by blending with BAL features. The reported uncertainties in the rest equivalent widths,  $\sigma_{W_r}$ , do not include errors associated with continuum normalization. The effect of uncertainties in continuum-level placement on the measurement of equivalent width can often be significant, especially for BAL quasars observed at the medium spectral resolution of our KCWI configuration. However, systematic errors in continuum placement are likely to be similar across the four sight lines. We therefore expect the analysis of the relative variation in  $W_r$  at a given  $z_{\text{abs}}$  to be insensitive to these uncertainties.

The strongest metal absorber in our sample (the  $W_{r,2796} = 0.98 \text{ \AA}$  Mg II system at  $z_{\text{abs}} = 0.7583$ ) is securely detected only in sight line D. As the observed wavelength range of this system overlaps with that of the  $z_{\text{abs}} = 2.177$  C IV system detected in sight lines A–C, we report an upper limit on  $W_{r,2796}$  at  $z_{\text{abs}} = 0.7583$  in these latter sight lines by first computing the boxcar  $W_r$  and  $\sigma_{W_r}$  over the velocity range assigned to this system in sight line D, and then computing the sum of  $W_r + 3 \sigma_{W_r}$ . These limits are likewise included in Table 1.

We show sections of our QSO spectroscopy surrounding the C IV absorption systems listed in Table 1 in Figure 3, and show the spectroscopy of systems exhibiting Fe II and/or Mg II absorption in Figure 4. Each spectrum is color coded to indicate

the corresponding QSO image (red, orange, green, and blue for images A, B, C, and D, respectively). Unassociated absorption features are indicated with dotted histograms. Figure 3 demonstrates the strong similarity between the C IV line profiles for our highest-redshift systems (at  $z > 2$ ), while the system at  $z \approx 1.76$  exhibits a significant change in absorption depth in sight line D versus A, B, and C. The velocity structure of the low-ion absorption shown in Figure 4 tends to vary more significantly from sight line to sight line, with two of the systems (at  $z = 0.577$  and  $z = 1.049$ ) exhibiting a velocity shear of  $\gtrsim 100$  km  $s^{-1}$ , and with all of the systems exhibiting significant differences in the depth of the line profile in at least one transition.

Given the complexity of the spectra of J014710+463040 and the resolution of these data, we do not attempt to identify metal absorption lines in the Ly $\alpha$  forest, and we are likely missing absorption lines contaminated by the BAL features dominating the regions near the quasar emission lines. Higher resolution data will be required to perform a comprehensive analysis of intervening absorption; however, we discuss some preliminary findings based on the present data set in Section 3.4.

The KCWI data were not of sufficient depth to detect emission from the lensing galaxy, and hence cannot directly constrain its redshift. We note that three intervening absorbers are found to have redshifts within the  $\pm 1\text{-}\sigma$  photometric errors of the Berghea et al. (2017) redshift estimate for the lens ( $z_L = 0.57^{+0.20}_{-0.13}$ ); in addition, two of these systems are detected in all four source images. One of these latter systems, identified at  $z_{\text{abs}} = 0.5775$  in sight line A, has a redshift very close to the best-fit photometric estimate. Moreover, source image D (the

**Table 1**  
Intervening Absorption-line Systems

Sight Line	Redshift	Transition ( $\lambda_r$ ) (Å)	$W_r$ (mÅ)	$\sigma_{W_r}$ (mÅ)
A	0.5775	Mg II 2796	111.1	5.2
A		2803	77.8	5.6
A	0.6069	Mg II 2796	462.1	5.0
A		2803	319.7	5.2
A		Fe II 2600	76.3 <sup>a</sup>	3.1
A	0.7583	Mg II 2796	...	<84.9 <sup>b</sup>
A		2803	...	<25.5 <sup>b</sup>
A	1.0491	Fe II 2600	185.0	3.9
A	1.5654	Al II 1670	17.0	2.6
A	1.7526	C IV 1548	99.9	2.3
A		1550	21.4	2.3
A	1.7588	C IV 1548	90.4	2.4
A		1550	66.9	2.5
A	2.0370	C IV 1548	130.5	2.0
A		1550	73.2	2.2
A		Si IV 1393	59.9	2.1
A		H I 1216	1749.7	5.0
A	2.0388	C IV 1548	52.9	1.9
A		1550	18.2	1.9
A	2.1766	C IV 1548	24.5	2.8
A		1550	3.4	2.9
B	0.5776	Mg II 2796	113.8	5.3
B		2803	56.9	5.7
B	0.6069	Mg II 2796	281.4	6.3
B		2803	60.2	6.5
B		Fe II 2600	18.9 <sup>a</sup>	3.4
B	0.7583	Mg II 2796	...	<79.2 <sup>b</sup>
B		2803	...	<48.0 <sup>b</sup>
B	1.0491	Fe II 2600	71.4	4.6
B	1.5650	Al III 1854	56.4	3.3
B		1862	38.8	3.3
B		Al II 1670	72.4	3.6
B	1.7586	C IV 1548	96.8	3.0
B		1550	67.8	2.9
B	2.0370	C IV 1548	108.1	2.4
B		1550	55.8	2.7
B		Si IV 1393	74.9	2.6
B		H I 1216	1866.1	4.9
B	2.0388	C IV 1548	23.6	2.2
B		1550	14.8	2.3
B	2.1767	C IV 1548	29.9	2.9
B		1550	21.1	3.0
C	0.5772	Mg II 2796	150.2	7.8
C		2803	94.0	8.0
C	0.6068	Mg II 2796	373.6	7.2
C		2803	207.0	7.4
C		Fe II 2600	56.1 <sup>a</sup>	4.5
C	0.7583	Mg II 2796	...	<112.8 <sup>b</sup>
C		2803	...	<66.7 <sup>b</sup>
C	1.0494	Fe II 2600	463.6	6.4
C	1.5650	Al II 1670	19.9	3.6
C	1.7585	C IV 1548	141.9	3.8
C		1550	101.4	4.0
C	2.0370	C IV 1548	144.8	3.0
C		1550	50.4	3.2
C		Si IV 1393	77.1	2.9
C		H I 1216	1783.6	6.6
C	2.0387	C IV 1548	53.8	2.5
C		1550	13.5	2.7
C	2.1764	C IV 1548	41.6	4.3
C		1550	26.4	4.5
D	0.5762	Mg II 2796	125.2	17.0
D		2803	83.0	17.4

**Table 1**  
(Continued)

Sight Line	Redshift	Transition ( $\lambda_r$ ) (Å)	$W_r$ (mÅ)	$\sigma_{W_r}$ (mÅ)
D	0.5768	Mg II 2796	116.3	17.1
D		2803	62.3	17.8
D	0.6068	Mg II 2796	290.7	20.8
D		2803	107.7	20.9
D		Fe II 2600	18.1 <sup>a</sup>	12.2
D	0.7583	Mg II 2796	983.1	24.6
D		2803	731.5	25.1
D		Fe II 2600	699.1 <sup>a</sup>	24.5
D	1.0487	Fe II 2600	628.4	17.8
D	1.5657	Al III 1854	55.6	11.1
D		1862	46.9	10.6
D		Al II 1670	70.8	11.1
D	1.7587	C IV 1548	29.6	10.0
D		1550	-4.0	10.7
D	2.0370	C IV 1548	117.2	8.7
D		1550	68.2	8.9
D		Si IV 1393	96.1	8.8
D		H I 1216	1690.5	24.4
D	2.0387	C IV 1548	18.9	6.3
D		1550	3.7	7.3

**Notes.** The observed wavelength of most of these absorbers is indicated above the corresponding source image spectrum in Figure 2.

<sup>a</sup> This transition is slightly blended with BAL features.

<sup>b</sup> Limits are determined first by computing the boxcar  $W_r$  and  $\sigma_{W_r}$  over the velocity range for this line in sight line D and then computing the sum of  $W_r + 3 \sigma_{W_r}$ .

image closest to the expected position of the lens in projection) exhibits a two-component absorbing structure in the system near  $z_L = 0.57$  (having  $z_{\text{abs}} = 0.5762$  and  $0.5768$ ). These double components are not evident in any of the other sight lines at  $z_{\text{abs}} = 0.577$ , and are suggestive of the complex, multiple-component Mg II absorbers typically observed close to bright galaxies (e.g., Kacprzak et al. 2010; Chen et al. 2014). Sight line D also exhibits strong Mg II absorption at  $z_{\text{abs}} \approx 0.76$  that is not detected in the other sight lines (and for which we list upper limits in Table 1), raising the possibility that this  $z_{\text{abs}} \approx 0.76$  system is associated with the lensing galaxy. Without a spectrum of the lens itself, we cannot be certain of its redshift; however, the detection of absorption in every sight line at  $z_{\text{abs}} \approx 0.577$ , its complex velocity structure in sight line D, and the consistency of this redshift with photometric constraints from Berghea et al. (2017) leads us to adopt  $z_L = z_{\text{abs}} = 0.5768$  in our analysis below.

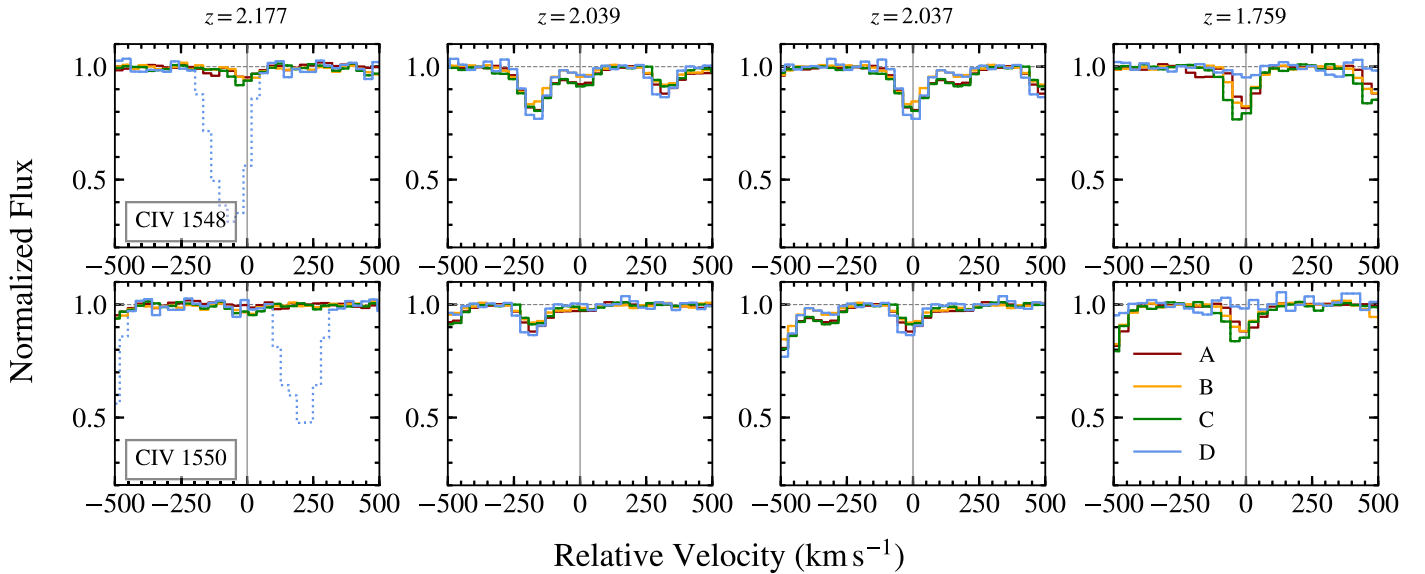
### 3.3. Sight Line Geometry

To compute the transverse separation of the four sight lines as a function of absorber redshift, we refer to Equation (5) in Cooke et al. (2010):

$$S_0 = \frac{\theta_{\text{obs}} D_L (D_S - D_{\text{abs}})}{(1 + z_{\text{abs}})(D_S - D_L)}, \quad (1)$$

where  $\theta_{\text{obs}}$  is the observed angular separation between the sight lines and  $D_X$  is the co-moving distance to the redshift  $z_X$ , with L, S, and “abs” indicating the lens, source, and absorber, respectively. For these calculations, we assume that the source is located directly behind the center of mass of the lensing galaxy.





**Figure 3.** Continuum-normalized lensed QSO spectroscopy centered on CIV  $\lambda\lambda 1548, 1550$  absorption in the high-redshift ( $z > 1.6$ ) intervening systems listed in Table 1 (excepting the system at  $z = 1.7526$  detected in sight line A). The red, orange, green, and blue spectra were extracted from QSO images A, B, C, and D, respectively. Relative velocities of  $0 \text{ km s}^{-1}$  correspond to the redshift centroid measured in sight line D (or in sight line A if the system is not detected in D). Strong absorption associated with material at a redshift other than that indicated above each column is indicated with dotted histograms.

Adopting  $z_L = 0.5768$  and a source redshift of  $z_S = 2.377$ , we show the resulting physical separations between all sight-line combinations at the redshifts of several of the systems identified in Section 3.2 in Table 2. If instead  $z_L = 0.6069$  or  $z_L = 0.7583$ , for systems with  $z_{\text{abs}} \geq z_L$  each distance would increase by a factor of 1.07 or 1.48, respectively<sup>12</sup>. The J014710+463040 system thus permits assessment of the variation in the strength and velocity structure of foreground absorption on scales of a kiloparsec at  $z_{\text{abs}} \approx 2$ ,  $\approx 5\text{--}10 \text{ kpc}$  at  $z_{\text{abs}} \approx 1$ , and  $\approx 10\text{--}20 \text{ kpc}$  at  $z_{\text{abs}} \approx 0.6$ .

### 3.4. Coherence in $W_r$ Across Multiple, Close Sight Lines

The analysis described in Section 3.2 revealed 7–9 securely detected intervening absorption systems toward every quasar image. For all of these systems, with the exception of the Al III absorbers, the CIV absorber at  $z_{\text{abs}} = 1.7526$  in sight line A, and the Mg II absorber at  $z_{\text{abs}} = 0.7583$  in sight line D, we detect counterpart absorbers within a velocity range of  $\delta v \pm 250 \text{ km s}^{-1}$ , with the vast majority of the counterparts lying within  $\delta v \pm 100 \text{ km s}^{-1}$ . Given the physical separation of the sight lines, this finding is suggestive of absorbing structures extending over relatively large scales (e.g.,  $> 5\text{--}20 \text{ kpc}$  at  $z_{\text{abs}} < 1$ ). To quantitatively assess the physical extent of these absorbers and the scale over which their  $W_r$  varies, we compute the fractional difference in  $W_r$  values measured at a given  $z_{\text{abs}}$  for each pair of sight lines,  $(W_{r,\text{ion}}^X - W_{r,\text{ion}}^Y) / W_{r,\text{ion}}^X$ , where sight line X has the stronger absorption of the two. We show these fractional differences for Mg II (filled circles) and Fe II (filled squares) systems in the upper left panel of Figure 5 versus the physical separation of the sight line pair (taken from Table 2). The lower left panel of the Figure shows the same measurements for our CIV systems (filled circles). Each point is color coded by the corresponding value of  $W_{r,\text{ion}}^X$ .

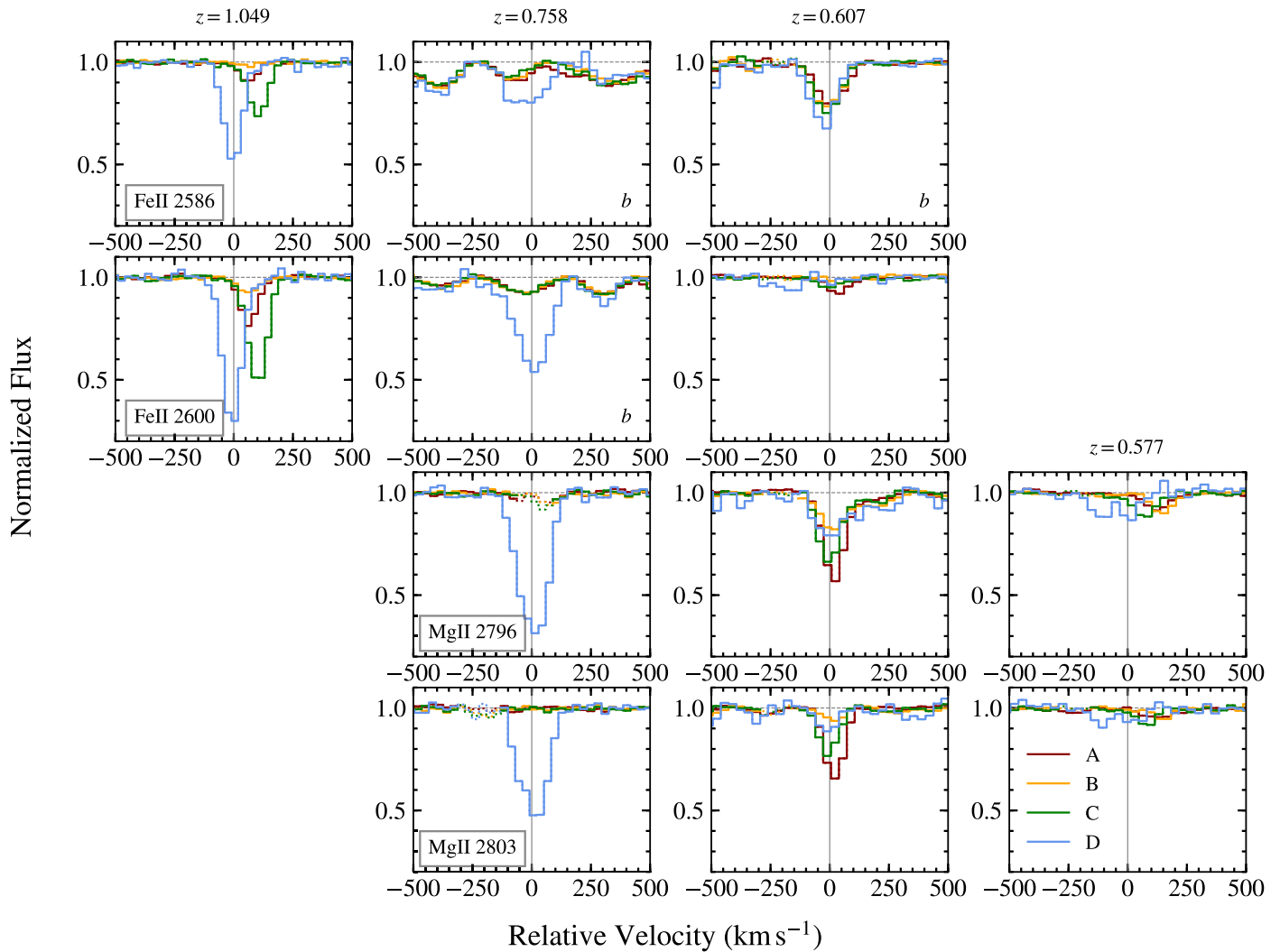
Considering the two Mg II systems at  $z_{\text{abs}} \approx 0.577$  and  $0.607$ , we measure small fractional  $W_{r,2796}$  differences ( $< 40\%$ ) across

the full range of sight-line separations ( $\sim 8\text{--}22 \text{ kpc}$ ), pointing to a high degree of coherence over large scales even for these relatively weak absorbers (having  $W_{r,2796} \approx 0.1\text{--}0.46 \text{ \AA}$ ). The much stronger ( $W_{r,2796} = 0.98 \text{ \AA}$ )  $z_{\text{abs}} \approx 0.758 \text{ Mg II}$  system, on the other hand, yields lower limits for fractional  $W_{r,2796}$  differences of  $\gtrsim 85\%$  at separations of  $\sim 17 \text{ kpc}$ .

The Fe II system at  $z_{\text{abs}} \approx 1.049$  on the whole exhibits larger absorption strength variations than our Mg II systems, yielding fractional  $W_{r,2600}$  differences of  $\approx 25\%\text{--}90\%$  between every sight line pair. We find that the four CIV systems likewise exhibit a quite high degree of variation, with  $W_{r,1548}$  differences ranging between  $\approx 5$  and  $80\%$  over  $0.3\text{--}3 \text{ kpc}$  separations. Such a wide range of  $W_{r,1548}$  values points to gas densities which vary on sub-kiloparsec scales for the weakest of these absorbers (with  $W_{r,1548} \sim 0.02\text{--}0.05 \text{ \AA}$ ).

Figure 5 also includes similar measurements collected from the literature analyzing intervening CIV 1548 and Mg II 2796 absorption along lensed quasar sight lines. For each system, we adopt updated constraints on  $z_L$  where available and recalculate the transverse physical sight-line separations assuming the WMAP5 cosmology (Komatsu et al. 2009, with one exception described below). In detail, we include systems from Young et al. (1981), Foltz et al. (1984), Smette et al. (1992, 1995), Crofts et al. (1994), Monier et al. (1998), Lopez et al. (1999, 2000), Ellison et al. (2004), Rogerson & Hall (2012), and Chen et al. (2014). For absorbers from Foltz et al. (1984), we assume  $z_L = 1.49$  and an angular sight-line separation of  $7''.13$  (Sol et al. 1984). In the case of absorbers from Smette et al. (1995), we assume  $z_L = 1$  as in Lopez et al. (1999). The Monier et al. (1998) study focused on the Cloverleaf lens, for which  $z_L$  is still not precisely known; here we adopt  $z_L = 1.88$  as estimated in Goicoechea & Shalyapin (2010). Rogerson & Hall (2012) reported  $W_{r,2796}$  measurements for spectra of the Einstein Cross published by Rauch et al. (2002), and for which we adopt astrometry from Crane et al. (1991). We also include Rogerson & Hall (2012) measurements for doubly and quadruply lensed quasar spectroscopy published by Churchill et al. (2003), Oguri et al. (2004, 2008), and Kayo et al. (2010).

<sup>12</sup> For the system at  $z_{\text{abs}} = 0.6069$ , if  $z_L = 0.7583$ , each distance would increase by the smaller factor of 1.07.



**Figure 4.** Continuum-normalized lensed QSO spectroscopy centered on Fe II  $\lambda\lambda 2586, 2600$  (top two rows) and Mg II  $\lambda\lambda 2796, 2803$  (bottom two rows) absorption in the  $z < 1.5$  systems listed in Table 1. As in Figure 3, spectra are color coded by the corresponding lens image. Relative velocities of  $0 \text{ km s}^{-1}$  correspond to the redshift centroid measured in sight line D. We do not show our spectroscopic coverage of the Fe II transitions associated with the  $z = 0.577$  system at  $\lambda_{\text{obs}} \sim 4100 \text{ \AA}$  as they fall among the intrinsic BAL features blanketing the Ly $\alpha$  emission line of the QSO. Spectroscopy shown in panels labeled with “b” at bottom right is affected by weaker BAL absorption.

**Table 2**  
Projected Distances between Lensed Sight Lines for  $z_L = 0.5768$

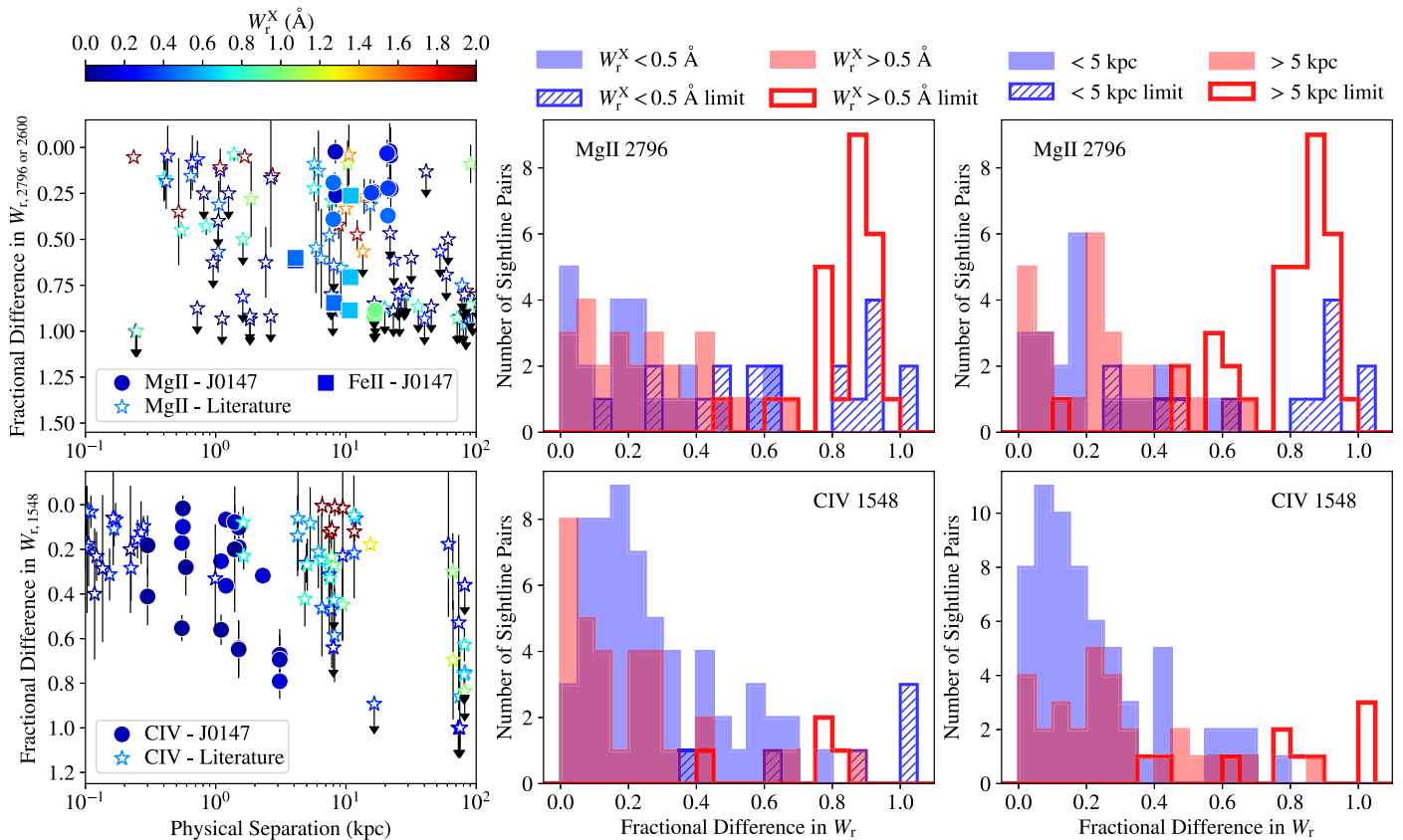
Sight Line Pair	$\theta_0$ ( $''$ )	$S_0(0.5768)$ (kpc)	$S_0(0.6069)$ (kpc)	$S_0(0.7583)$ (kpc)	$S_0(1.0491)$ (kpc)	$S_0(1.7588)$ (kpc)	$S_0(2.0370)$ (kpc)	$S_0(2.1766)$ (kpc)
A-B	1.26	8.3	8.0	6.4	4.1	1.2	0.55	0.30
A-C	1.27	8.4	8.0	6.4	4.1	1.2	0.56	0.30
A-D	3.34	22.0	21.0	16.8	10.8	3.1	1.5	0.79
B-C	2.48	16.4	15.7	12.5	8.1	2.3	1.1	0.59
B-D	3.28	21.7	20.7	16.5	10.7	3.1	1.4	0.78
C-D	3.35	22.1	21.1	16.8	10.9	3.1	1.5	0.80

For absorbers in paired sight lines listed in Rogerson & Hall (2012), as well as for all absorbers listed in Chen et al. (2014), we do not compute sight-line separations, and instead adopt the physical distances listed in those works (although they assume slightly different cosmological parameters).

The fractional  $W_r$  differences (or lower limits in cases in which an absorber is securely detected along only one sight line) for these systems are indicated with open stars in the left-hand panels of Figure 5. Here we exclude systems that yield fractional

$W_r$  differences or limits less than 0.0, as well as constraints for which the  $1\sigma$  uncertainty in the fractional  $W_r$  difference is greater than 0.5. We also exclude lower limits from the sample if they are  $< 0.05$ . After making these exclusions, the final sample of fractional  $W_r$  difference measurements includes constraints from 98 sight line pairs probing Mg II absorption and 104 sight line pairs probing C IV systems.

The predominant feature of both top and bottom left-hand panels in Figure 5 is the significant scatter over the full range of



**Figure 5.** Left panels: fractional difference in  $W_r$  as a function of sight-line separation at  $z_{\text{abs}}$  for intervening absorbers detected toward J014710+463040 (filled circles and squares) and toward lensed QSOs analyzed in previous studies (open stars; Young et al. 1981; Foltz et al. 1984; Smette et al. 1992; Crofts et al. 1994; Smette et al. 1995; Monier et al. 1998; Lopez et al. 1999, 2000; Ellison et al. 2004; Rogerson & Hall 2012; Chen et al. 2014). The fractional difference is  $(W_{r,\text{ion}}^X - W_{r,\text{ion}}^Y)/W_{r,\text{ion}}^X$ , where sight line X has the stronger absorption of the two systems. Points are color coded to indicate  $W_r^X$ , and the vertical scale increases top to bottom (i.e., more to less coherent). The upper panel shows  $W_r$  offsets in Mg II 2796 (filled circles and open stars) and Fe II 2600 (filled squares). The lower panel shows the same measurements for C IV 1548. Middle panels: frequency distributions of fractional difference values shown in the left-most panels. Sight line pairs with secure detections in both images are included in the solid histograms, and pairs which yield lower limits on the fractional difference are included at the value of the limit in the hatched and open histograms. Distributions shown in blue include systems with  $W_r^X < 0.5$  Å, and distributions shown in red include systems with  $W_r^X > 0.5$  Å. Right panels: same as middle panels, with blue histograms showing sight line pairs with separations of  $< 5$  kpc, and red histograms including sight line pairs at larger physical separations.

physical separations shown, pointing to a high degree of variation in the spatial coherence for both metal-line transitions. However, we also note a higher incidence of non-detections in paired sight lines probing Mg II absorption relative to the sample probing C IV systems, and that these non-detections arise frequently even among close sight line pairs.

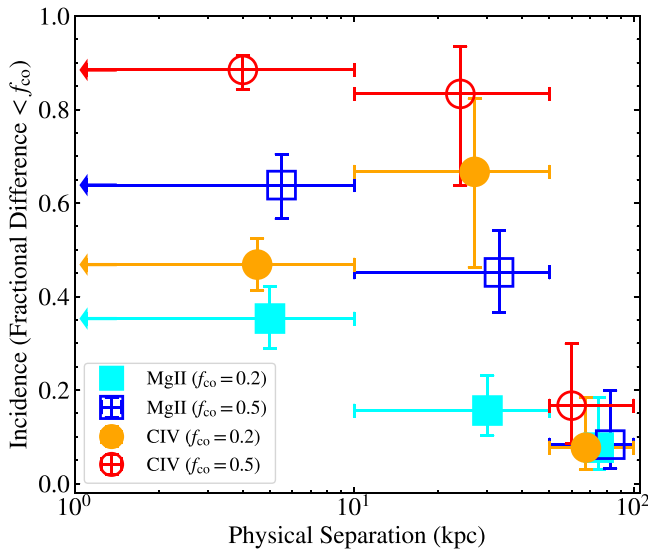
To make this comparison more explicit, the middle panels of Figure 5 show the distributions of these fractional  $W_r$  differences for subsamples having maximum  $W_r$  values  $< 0.5$  Å (in blue) and  $> 0.5$  Å (in red). Systems with secure detections in both sight lines are included in the solid histograms, and systems yielding lower limits on the fractional  $W_r$  difference are included in the open and hatched histograms. A total of 34 (or 35%) of the Mg II systems yield lower limits on the fractional  $W_r$  difference of  $> 0.75$ , while only 9 of the 104 total C IV systems exhibit such low fractional differences. To quantitatively assess the significance of the differences in these distributions, we use the Python package `lifelines`<sup>13</sup> to perform a survival analysis. Because our data set is characterized by left censorship (in that non-detections represent upper bounds), rather than comparing

the distributions of fractional  $W_r$  differences, we compare distributions of the quantity  $W_{r,\text{ion}}^Y/W_{r,\text{ion}}^X$  so that the censored data corresponds to upper limits. A log-rank test comparing the survival distributions of this ratio for the full Mg II versus C IV samples yields a p-value  $< 10^{-8}$ , ruling out the null hypothesis that these data sets are drawn from the same parent population.

However, for a given ion, a comparison of the red versus blue histograms in these middle panels is not suggestive of significantly different distributions. Log-rank tests performed as described above yield p-values of 0.32–0.48, and hence do not rule out the null hypothesis that the fractional  $W_r$  differences for subsamples divided by maximum  $W_r$  are drawn from the same parent population. We thus do not find evidence for a relationship between the degree of coherence and absorber strength.

The right-hand panels of Figure 5 show fractional  $W_r$  difference distributions for subsamples with sight line separations  $< 5$  kpc (blue) and  $> 5$  kpc (red). The C IV systems in particular have small fractional differences with much higher frequency at small separations. Log-rank tests yield p-values of 0.055 and  $< 10^{-4}$  for the Mg II and C IV distributions, respectively, thus securely ruling out the null hypothesis that subsamples at  $< 5$  kpc versus  $> 5$  kpc separations are drawn

<sup>13</sup> Available at <https://github.com/CamDavidsonPilon/lifelines>.



**Figure 6.** Incidence rate of fractional  $W_r$  differences less than a given coherence limit ( $f_{co}$ ) in three bins of sight-line separation. Incidence rates for Mg II 2796 absorbers are indicated in solid cyan (for  $f_{co} = 0.2$ ) and open blue (for  $f_{co} = 0.5$ ) squares, and incidence rates for C IV 1548 absorbers are plotted in solid orange and open red circles. The horizontal error bars show the range in physical separation included in each bin, and the x-axis location of each point has been slightly offset from the corresponding bin midpoint to improve legibility. Vertical error bars show the  $\pm 34$ th percentile Wilson score confidence intervals. While both  $W_{r,2796}$  and  $W_{r,1548}$  vary by  $<20\%$  in about half of the sight line pairs within  $<10$  kpc, such a high degree of coherence is rare among Mg II systems at  $>10$  kpc separations.

from the same parent population in the case of the latter transition.

An alternative way of assessing the degree of coherence of a set of absorbers as a function of physical distance is to consider the frequency with which the absorbers exhibit fractional  $W_r$  differences lower than a given coherence level,  $f_{co}$ . In Figure 6, we show the fraction of absorbers having fractional  $W_r$  differences lower than  $f_{co} = 0.2$  and  $f_{co} = 0.5$  in subsamples with physical separations  $<10$  kpc, between 10 and 50 kpc, and  $>50$  kpc. Within 10 kpc, 64% of the sample Mg II systems have fractional  $W_{r,2796}$  differences of  $<0.5$ , and 35% have fractional  $W_{r,2796}$  differences of  $<0.2$ . At separations greater than 10 kpc, fractional  $W_{r,2796}$  differences  $<0.2$  are more infrequent; however, fractional  $W_{r,2796}$  differences  $<0.5$  persist in nearly half of the systems. Such small  $W_r$  variations are suggestive of Mg II-absorbing clouds or cloud complexes extending over areas several kiloparsecs across for both strong and weak Mg II systems.

C IV systems exhibit a yet higher degree of coherence, with  $\approx 80\text{--}90\%$  of systems having fractional  $W_{r,1548}$  differences  $<0.5$  out to physical separations of 50 kpc, and with  $\approx 45\text{--}70\%$  of systems varying by  $<20\%$  over the same scales. It is only beyond separations of 50 kpc that the incidence of coherent absorption drops to  $<20\%$  (and is comparably low for both transitions). Indeed, this analysis is suggestive of a scenario in which it is common for C IV absorption to fluctuate by  $<20\%$  over the scale subtended by a typical host dark matter halo (hosting, e.g., a Lyman Break Galaxy with virial radius  $<90$  kpc; Adelberger et al. 2005; Steidel et al. 2010).

#### 4. Discussion

The study of intervening absorption-line systems observed in background quasar spectroscopy has proven essential for

assessing, e.g., the neutral gas content of the Universe (Wolfe et al. 2005) and the evolution of its metal content (Simcoe et al. 2011; Lehner et al. 2014). In spite of these advances, numerous open questions remain regarding the physical nature of the absorbers themselves. Cosmological simulations predict that many of these systems arise in the environments of luminous galaxies, tracing cool inflowing streams or large-scale outflows driven by star formation (e.g., Fumagalli et al. 2011; Shen et al. 2013; Faucher-Giguère et al. 2015). However, it has proven difficult to leverage such predictions for constraints on the physical origins of a given observed absorber population.

A crucial limitation has been our lack of information on the sizes and morphologies of the absorbing structures. Because background quasars provide only a pencil-beam probe, constraints on the physical extent of these systems have been obtained via modeling of the ionization state of the gas (Churchill & Charlton 1999; Stocke et al. 2013; Werk et al. 2014). However, these analyses are subject to substantial systematic uncertainties (e.g., in the shape of the extragalactic ionizing background spectrum and in the cloud geometry/density profile), and typically may only be used to constrain the cloud thickness to within an order of magnitude (e.g., Werk et al. 2014).

Spectroscopy of multiple, close background sight lines offers a valuable alternative probe of absorber morphology by mapping the transverse dimension. Gravitationally lensed quasars are perhaps the most efficient such sources, as they may be very bright and produce similar continua at a given  $\lambda_{obs}$ . These unique sources have been used in numerous previous studies to probe the scale of variations in absorption strength (e.g., Smette et al. 1995; Monier et al. 1998; Rauch et al. 1999, 2001, 2002; Ellison et al. 2004). In particular, Ellison et al. (2004) and Rogerson & Hall (2012) have presented compilations of such measurements from the literature, and have used these data sets to constrain the coherence length of the absorbers under the assumption of spherical clouds (in the former) and in the context of the Tinker & Chen (2008) gaseous halo model (in the latter). The Ellison et al. (2004) analysis points to coherence lengths  $>3$  kpc for both highly ionized systems and for strong ( $W_{r,2796} > 0.3$  Å) Mg II systems, and suggests shorter coherence lengths for weaker low-ionization absorption systems. These findings are qualitatively consistent with the present analysis (which includes some of the same data along with a supplemental sample of lensed sight lines at separations  $>5$  kpc). Overall, the  $W_r$  variations observed in these systems indicate that either (1) each gas cloud composing the absorbers extends across the physical separation of the beams, or (2) they arise from extended structures made up of numerous smaller clouds with similar velocity spread and/or column density along any given sight line.

Ultimately, higher spectral resolution ( $\mathcal{R} > 6000$ ) will be required to distinguish between these scenarios, as it permits detailed comparison of the column densities, velocity centroids, and line widths of individual absorbing components across the sight lines (e.g., Rauch et al. 1999, 2001, 2002; Chen et al. 2014). Indeed, such studies have already provided evidence for variation in velocity structure on sub-kiloparsec scales in the case of low-ionization absorption (e.g., Rauch et al. 2002) and on scales of kiloparsecs in the case of high-ionization absorbers (e.g., Smette et al. 1995; Rauch et al. 2001). A spectroscopic survey for galaxies associated with these absorbers will allow us to establish their context within the CGM, and will, in addition, test a basic assumption invoked by most CGM studies



to date. Mg II absorbers with strengths similar to those in our sample (with  $W_r,2796 \approx 0.1\text{--}1 \text{ \AA}$ ) are common within projected distances of  $R_\perp < 50 \text{ kpc}$  of  $\sim L^*$  galaxies at low redshift ( $z \sim 0.2$ ; Chen et al. 2010). However, constraints on the  $W_r,2796$  distribution in these environments come from the assembly of numerous projected QSO-galaxy pairs, each of which probes an independent halo. Larger samples of lensed QSOs probing foreground systems (e.g., Chen et al. 2014; Zahedy et al. 2016) will provide a critical test of the standard interpretation that the  $W_r$  distribution of absorbers observed toward an ensemble of QSO-galaxy pairs is representative of the absorption profile in an individual galaxy CGM.

Moreover, measurement of the sizes, velocity coherence, and metallicity of such absorbers will permit quantitative comparisons to the CGM features predicted in hydrodynamical zoom simulations, differentiating between smooth accretion streams, gas associated with infalling satellites, and the turbulent, clumpy flows arising from stellar feedback (e.g., Shen et al. 2013; Faucher-Giguère et al. 2015; Nelson et al. 2015; Fielding et al. 2017). Such constraints will, in addition, be necessary to assess the susceptibility of these structures to destruction by hydrodynamic instabilities, and hence will reveal their survival timescale (e.g., Crighton et al. 2015; McCourt et al. 2018). With  $>2000$  lensed QSOs expected to be discovered in the ongoing PS1 and Dark Energy Surveys (Dark Energy Survey Collaboration et al. 2016), and several thousand to be uncovered by the Large Synoptic Survey Telescope (Ivezic et al. 2008; Oguri & Marshall 2010), this technique will soon become the state of the art in CGM studies.





K.L.C. acknowledges support from NSF grant AST-1615296. The authors wish to thank Jessica Werk and Dylan Nelson for illuminating discussions of these results, and we thank Jessica Werk for her reading and critique of this manuscript. The data presented herein were obtained at the W. M. Keck Observatory, which is operated as a scientific partnership among the California Institute of Technology, the University of California, and the National Aeronautics and Space Administration. The Observatory was made possible by the generous financial support of the W. M. Keck Foundation.

The authors wish to recognize the very significant cultural role and reverence that the summit of Maunakea has always had within the indigenous Hawaiian community. We are most fortunate to have the opportunity to conduct observations from this mountain.

Finally, the authors dedicate this work to the memory of Jerry Nelson, without whom the immense contributions to science made by the Keck Observatory would not be possible.

*Facility:* Keck:II (KCWI).

### ORCID iDs

Kate H. R. Rubin  <https://orcid.org/0000-0001-6248-1864>  
 John M. O’Meara  <https://orcid.org/0000-0002-7893-1054>  
 Luca Rizzi  <https://orcid.org/0000-0003-0882-2327>  
 James D. Neill  <https://orcid.org/0000-0002-0466-1119>

### References

Adelberger, K. L., Shapley, A. E., Steidel, C. C., et al. 2005, *ApJ*, 629, 636  
 Bergeron, J., & Stasińska, G. 1986, *A&A*, 169, 1

Berghea, C. T., Nelson, G. J., Rusu, C. E., Keeton, C. R., & Dudik, R. P. 2017, *ApJ*, 844, 90  
 Bonvin, V., Courbin, F., Suyu, S. H., et al. 2017, *MNRAS*, 465, 4914  
 Chambers, K. C., Magnier, E. A., Metcalfe, N., et al. 2016, arXiv:1612.05560  
 Chen, H.-W., Gauthier, J.-R., Sharon, K., et al. 2014, *MNRAS*, 438, 1435  
 Chen, H.-W., Helsby, J. E., Gauthier, J.-R., et al. 2010, *ApJ*, 714, 1521  
 Churchill, C. W., & Charlton, J. C. 1999, *AJ*, 118, 59  
 Churchill, C. W., Mellon, R. R., Charlton, J. C., & Vogt, S. S. 2003, *ApJ*, 593, 203  
 Cooke, R., Pettini, M., Steidel, C. C., et al. 2010, *MNRAS*, 409, 679  
 Crane, P., Albrecht, R., Barbieri, C., et al. 1991, *ApJL*, 369, L59  
 Crighton, N. H. M., Hennawi, J. F., Simcoe, R. A., et al. 2015, *MNRAS*, 446, 18  
 Crots, A. P. S., Bechtold, J., Fang, Y., & Duncan, R. C. 1994, *ApJL*, 437, L79  
 Dark Energy Survey Collaboration, Abbott, T., Abdalla, F. B., et al. 2016, *MNRAS*, 460, 1270  
 Diehl, H. T., Abbott, T. M. C., Annis, J., et al. 2014, *Proc. SPIE*, 9149, 91490V  
 Ellison, S. L., Ibata, R., Pettini, M., et al. 2004, *A&A*, 414, 79  
 Faucher-Giguère, C.-A., Hopkins, P. F., Kereš, D., et al. 2015, *MNRAS*, 449, 987  
 Fielding, D., Quataert, E., McCourt, M., & Thompson, T. A. 2017, *MNRAS*, 466, 3810  
 Foltz, C. B., Weymann, R. J., Roser, H.-J., & Chaffee, F. H., Jr. 1984, *ApJL*, 281, L1  
 Fumagalli, M., Prochaska, J. X., Kasen, D., et al. 2011, *MNRAS*, 418, 1796  
 Goicoechea, L. J., & Shalyapin, V. N. 2010, *ApJ*, 708, 995  
 Hewett, P. C., & Wild, V. 2010, *MNRAS*, 405, 2302  
 Inada, N., Oguri, M., Shin, M.-S., et al. 2012, *AJ*, 143, 119  
 Ivezic, Z., Axelrod, T., Brandt, W. N., et al. 2008, *SerAJ*, 176, 1  
 Kacprzak, G. G., Churchill, C. W., Ceverino, D., et al. 2010, *ApJ*, 711, 533  
 Kayo, I., Inada, N., Oguri, M., et al. 2010, *AJ*, 139, 1614  
 Kochanek, C. S., Mochejska, B., Morgan, N. D., & Stanek, K. Z. 2006, *ApJL*, 637, L73  
 Komatsu, E., Dunkley, J., Nolta, M. R., et al. 2009, *ApJS*, 180, 330  
 Lehner, N., O’Meara, J. M., Fox, A. J., et al. 2014, *ApJ*, 788, 119  
 Lopez, S., Hagen, H.-J., & Reimers, D. 2000, *A&A*, 357, 37  
 Lopez, S., Reimers, D., Rauch, M., Sargent, W. L. W., & Smette, A. 1999, *ApJ*, 513, 598  
 McCourt, M., Oh, S. P., O’Leary, R., & Madigan, A.-M. 2018, *MNRAS*, 473, 5407  
 Monier, E. M., Turnshek, D. A., & Lupie, O. L. 1998, *ApJ*, 496, 177  
 Nelson, D., Genel, S., Vogelsberger, M., et al. 2015, *MNRAS*, 448, 59  
 Nemiroff, R. J. 1988, *ApJ*, 335, 593  
 Oguri, M., Inada, N., Keeton, C. R., et al. 2004, *ApJ*, 605, 78  
 Oguri, M., & Marshall, P. J. 2010, *MNRAS*, 405, 2579  
 Oguri, M., Ofek, E. O., Inada, N., et al. 2008, *ApJL*, 676, L1  
 Rauch, M., Sargent, W. L. W., & Barlow, T. A. 1999, *ApJ*, 515, 500  
 Rauch, M., Sargent, W. L. W., & Barlow, T. A. 2001, *ApJ*, 554, 823  
 Rauch, M., Sargent, W. L. W., Barlow, T. A., & Simcoe, R. A. 2002, *ApJ*, 576, 45  
 Rogerson, J. A., & Hall, P. B. 2012, *MNRAS*, 421, 971  
 Schechter, P. L., Morgan, N. D., Chehade, B., et al. 2017, *AJ*, 153, 219  
 Shanks, T., Metcalfe, N., Chehade, B., et al. 2015, *MNRAS*, 451, 4238  
 Shen, S., Madau, P., Guedes, J., et al. 2013, *ApJ*, 765, 89  
 Simcoe, R. A., Cooksey, K. L., Matejek, M., et al. 2011, *ApJ*, 743, 21  
 Sluse, D., Hutsemékers, D., Courbin, F., Meylan, G., & Wambsganss, J. 2012, *A&A*, 544, A62  
 Smette, A., Robertson, J. G., Shaver, P. A., et al. 1995, *A&AS*, 113, 199  
 Smette, A., Surdej, J., Shaver, P. A., et al. 1992, *ApJ*, 389, 39  
 Sol, H., Vanderriest, C., Schneider, J., Lelievre, G., & Pedersen, H. 1984, *A&A*, 132, 105  
 Steidel, C. C., Erb, D. K., Shapley, A. E., et al. 2010, *ApJ*, 717, 289  
 Stocke, J. T., Keeney, B. A., Danforth, C. W., et al. 2013, *ApJ*, 763, 148  
 Tinker, J. L., & Chen, H.-W. 2008, *ApJ*, 679, 1218  
 Werk, J. K., Prochaska, J. X., Tumlinson, J., et al. 2014, *ApJ*, 792, 8  
 Weymann, R. J., Morris, S. L., Foltz, C. B., & Hewett, P. C. 1991, *ApJ*, 373, 23  
 Wisotzki, L., Becker, T., Christensen, L., et al. 2003, *A&A*, 408, 455  
 Wolfe, A. M., Gawiser, E., & Prochaska, J. X. 2005, *ARA&A*, 43, 861  
 Young, P., Sargent, W. L. W., Oke, J. B., & Boksenberg, A. 1981, *ApJ*, 249, 415  
 Zahedy, F. S., Chen, H.-W., Rauch, M., Wilson, M. L., & Zabludoff, A. 2016, *MNRAS*, 458, 2423